MIXING AND WARMING OF CRYOGENIC HYDROGEN RELEASES

Ethan S. Hecht[a], Pratikash P. Panda[b]

[a]Combustion Research Facility, Sandia National Laboratories, P.O. Box 969, MS 9052, Livermore, CA, 94551, USA, ehecht@sandia.gov

[b]Fire Dynamics Research Group, FM Global, Norwood, MA, 02062, USA

ABSTRACT

Laboratory measurements were made on the concentration and temperature fields of cryogenic hydrogen jets. Images of spontaneous Raman scattering from a pulsed planar laser sheet were used to measure the concentration and temperature fields from varied releases. Jets with up to 5 bar pressure, with near-liquid temperatures at the release point, were characterized in this work. This data is relevant for characterizing unintended leaks from piping connected to cryogenic hydrogen storage tanks, such as might be encountered at a hydrogen fuel cell vehicle fueling station. The average centerline mass fraction was observed to decay at a rate similar to room temperature hydrogen jets, while the half-width of the Gaussian profiles of mass fraction were observed to spread more slowly than for room temperature hydrogen. This suggests that the mixing and models for cryogenic hydrogen may be different than for room temperature hydrogen. Results from this work were also compared to a one-dimensional (streamwise) model. Good agreement was seen in terms of temperature and mass fraction. In subsequent work, a validated version of this model will be exercised to quantitatively assess the risk at hydrogen fueling stations with cryogenic hydrogen on-site.

1.0 INTRODUCTION

Hydrogen is increasingly being used in the public sector as a fuel for vehicles, with ambitious targets for growth. In California, the network of 26 hydrogen fueling stations open in June, 2016, is projected to expand to 50 by the end of 2017 [1]. Aggressive construction of fueling stations is needed to support the growing number of fuel cell electric vehicles, with over 10,000 vehicles expected in 2018, and over 40,000 vehicles expected in 2022 [1]. Urban centers, including San Francisco, Los Anglels, and San Diego (in California, with additional urban centers on the east coast such as Boston and New York) will need to have large fueling stations, able to dispense fuel to many vehicles daily. In order to have sufficient hydrogen on-site (300-600 kg/day), and a sustainable method of hydrogen delivery, hydrogen at many stations will likely be delivered and stored as a liquid.

The fire codes that govern hydrogen use, such as NFPA 2: Hydrogen Technologies Code [2], have challenging separation distance requirements for liquid hydrogen. The density of liquid hydrogen at 1-5 bar (a typical storage tank operating pressure) is approximately 70 kg/l, so in order to have 1000 kg hydrogen on a site a station would need to have a tank of approximately 15,000 l. A tank of this size (13,251–56,781 l), as specified in NFPA 2 [2], requires 15 m of separation from lot lines, ignition sources, sprinklered buildings of combustible construction, and overhead utilities, and 23 m of separation from building openings, places of public assembly, unsprinklered buildings of combustible construction, and other combustible liquids or gases (e.g., gasoline tanks). While fire barrier walls can be used to reduce separation distances to lot lines, buildings, and other combustible liquids or gases, there are no mitigations for reducing the 23 m separation distance to building openings/air intakes or places of public assembly, or the 15 m separation distance from ignition sources or overhead utilities. The 23 m separation distance

can be especially challenging to meet in urban centers, where the high vehicle throughput necessitates large quantities of hydrogen storage.

As discussed in Annexes E and I of NFPA 2 [2], the separation distances for gaseous hydrogen are based on a risk-informed process, much of which is described by LaChance [3] and LaChance et al. [4]. This risk-informed process relies on data of leak frequency and size coupled to behavior models of hydrogen flames that result in heat radiation causing harm or fatalities to personnel at the site. In order to perform these analyses for liquid hydrogen systems such that the separation distances can be modified (hopefully reduced) based on scientific analyses, validated behavior models for cryogenic hydrogen are needed, analogous to the models used in the risk-based process for gaseous hydrogen. As described in Panda and Hecht [5], we began this work by studying at the ignition and flame characteristics of cryogenic hydrogen releases.

In this work, we focus on the unignited concentration fields of cryogenic hydrogen releases. In NFPA 2 [2], some of the separation distances are based on the 8% concentration boundary of ungnited releases, and therefore we need models to be able to predict this boundary for a range of release scenarios. Xiao et al. [6] describe experiments at an FZK facility where the centerline concentration decay of hydrogen from a 298 and 80 K reservoir flowing through 1–2 mm diameter nozzles was measured. The authors were able to show good agreement with an integral model. Freidrich et al. [7] describe experiments at the Karlsruhe Institute of Technology where the concentration was measured at some discrete points along the centerline of hydrogen releases for 34–65 K hydrogen at up to 30 bar. They found that the concentration decayed slower than for the warmer (290 and 80 K releases). Other than these two experiments, there is a dearth of data suitable for hydrogen concentration modeling validation.

Winters and Houf [8, 9] developed a model for simulating liquid hydrogen releases. While this model compared favorably to the Xiao et al. data [6], it has not been investigated for its suitability for releases of hydrogen at temperatures below 80 K. Further, only the centerline concentration predictions were compared to experiments, and the rate of hydrogen dispersion radially has not been studied. In this work, we have investigated the dispersion of hydrogen with a reservoir temperature of 50–64 K. We have measured the 2-dimensional concentration fields and compared this to the Winters and Houf model.

2.0 EXPERIMENTAL DESCRIPTION

The cryogenic hydrogen release platform, as described by Panda and Hecht [5] was used to generate releases of ultra-cold hydrogen in the laboratory. Briefly, gaseous hydrogen was cooled in a vacuum jacketed heat exchanger, first by liquid nitrogen, then by cold gaseous helium, and finally by liquid helium. This ultra-cold hydrogen, which was liquefied at the exit of the heat exchanger in some cases, flowed into the lab through a single vacuum jacketed line. A pressure transducer just before the interchangeable orifices (of 1.0 and 1.25-mm diameter) was used in a feedback loop to control the pressure of the release. A set of silicone diode temperature sensors just before the orifice were used to characterize the temperature of the hydrogen. A co-flow of air through a 19 cm diameter honeycomb at 0.3 m/s surrounded the cold hydrogen, to minimize the effect of any spurious room currents. A square 80×80 cm square hood located approximately 70 cm above the laser sheet exhausted the gases. Typical exhaust volumes were 100 l/min, giving a face velocity of around 2–2.5 m/s.

A sketch of the diagnostic setup is shown in Fig. 1. Two cameras on a single side of the cryogenic releases capture light scattered from a frequency doubled Nd:YAG laser (532-nm, 9-ns pulse 700-mJ/pulse) that was focused into an approximately 18-mm high sheet using a spherical plano-convex ($f = 1000$-mm) and a cylindrical plano-concave ($f = -200$-mm) lens pair. The cameras were set up to capture Raman scattered light from nitrogen and hydrogen. The nitrogen camera was a PIMAX ICCD operated with a gain of 255 and cropped to approximately 1/3 of the height. The hydrogen camera was an unintensified PIXIS 400B operated with 4×4 on-chip binning. The intensified (nitrogen) camera had its lenses slightly offset using the Scheimpflug principle, so that the entire image plane was in focus. Both cameras were outfitted with a Nikon 50-mm lens, each with a Nikon 3T close up lens and an OD 6, 532-nm, 17-nm FWHM

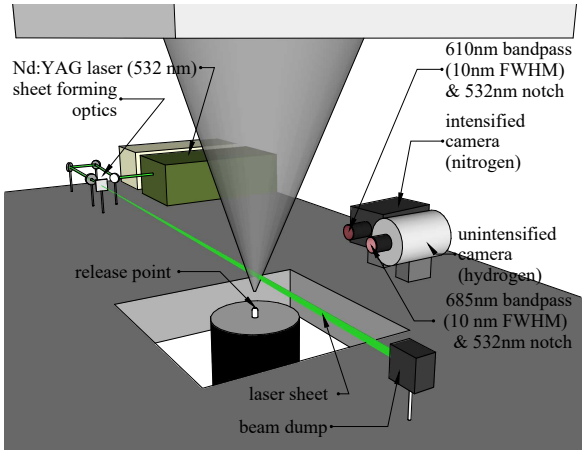

Figure 1. Diagnostic setup of experiment. A frequency doubled Nd:YAG laser is formed into a sheet, and Raman signals at two specific wavelengths are collected simultaneously by two cameras.

notch filter to block out the laser light. Both cameras were filtering out light except for the Stokes-shifted spontaneous Raman scattering from the desired gas molecules, accomplished by including a stack of three OD 4 10-nm FWHM bandpass filters; nitrogen with the passband centered at 610-nm to capture the Raman light at 607 nm, and hydrogen with the passband centered at 685-nm to capture the Raman light at 683-nm.

Spontaneous Raman shifted scattering is proportional to the concentration of each gas and the intensity of the incident laser light. The proportionality constant is a function of the cross-section of the gas molecules as well as the collection efficiency and response of the camera and optics system. To linearize the response of the lens and camera systems (such that the signals would be proportional to the amount of Raman light), calibrations were first performed on each lens and camera system [10]. With the same optics in place, a pure flow of either hydrogen or nitrogen was generated, and Raman signals were collected. The signals were corrected for the laser sheet intensity by dividing by the average laser power in the horizontal direction. Then at each (binned, for the unintensified camera) pixel location, a functional fit was found to relate the counts to the intensity of light. Rather than using higher order polynomial to fit the response, as described by Williams and Shaddix [10], a single proportionality constant was found for the camera systems in this case, due to the facts that we were not using much of the dynamic range of the cameras for the small Raman signals, and the unintensified camera would be expected to be nominally linear. This calibration method corrected for the unequal response for each (possibly binned) camera pixel, and vignetting that was observed towards the edges of each image.

We assume in this analysis that the releases are at atmospheric pressure (since we are not attempting to measure within the expansion zone of these releases), and that the ideal gas law can be used to relate the concentration of the gases to the mole fraction and temperature. We also assume that the temperature dependent cross-section changes are negligible, which should be valid for the low-temperature flows in this work. Mathematically, the intensity of Raman light can therefore be represented by the equations

$$I_{\mathrm{H_2}} = k_{\mathrm{H_2}} I_0 \frac{x_{\mathrm{H_2}}}{T} \tag{1}$$

$$I_{\mathrm{N_2}} = k_{\mathrm{N_2}} I_0 \frac{x_{\mathrm{N_2}}}{T}, \tag{2}$$

where $k_{\mathrm{H_2}}$ or $k_{\mathrm{N_2}}$ is a proportionality constant for each camera and lens system that includes the cross-section of the gas molecule, the collection efficiency and response of the camera system. We also stipulate that the mole fractions of hydrogen and air must sum to one, or $x_{\mathrm{H_2}} + 1.28 x_{\mathrm{N2}} = 1$, where the factor 1.28 comes from the fact that air is 78% nitrogen. Calibrations were performed to determine the proportionality constant for each camera to the gas of interest (H_2 or N_2). An

Table 1. Experimental conditions in this work.

T_{noz} (K)	P_{noz} (bar_{abs})	d_{noz} (mm)	$n_{heights}$	T_{throat} (K)	P_{throat} (bar_{abs})	ρ_{throat}	v_{throat} (m/s)
58	2.0	1.0	4	43.5	0.972	0.55	544.5
56	3.0	1.0	4	41.9	1.457	0.86	533.3
53	4.0	1.0	4	39.6	1.940	1.22	516.4
50	5.0	1.0	5	37.4	2.422	1.65	498.2
61	2.0	1.25	6	45.7	0.973	0.52	558.9
51	2.5	1.25	2	38.2	1.215	0.79	508.4
51	3.0	1.25	6	38.2	1.457	0.95	507.5
55	3.5	1.25	3	41.2	1.699	1.03	527.6
54	4.0	1.25	2	40.4	1.940	1.20	521.6

area of pure hydrogen was generated in the lab using a laminar coflow box and Raman signals were collected by both cameras. The area of hydrogen was surrounded by a coflow of pure nitrogen, enabling signal differentiation between air and nitrogen. Because the signals were corrected to scale the intensity of pure air a value of 1, the calibration constant for nitrogen was found to be $k_{N_2} = 1.28 \cdot 295$ K. The calibration constant for hydrogen was found to be $k_{H_2} = 2.05 \cdot 293$ K. A target was imaged by both cameras and the known geometry of the target image was used to align both camera images and scale them to true spatial dimensions. There were approximately 1.7 (4×4 binned) pixels per mm for the unintensified (hydrogen) camera, and approximately 4.6 pixels per mm for the intensified (nitrogen) camera.

The signal detected by each camera is composed of electronic background (the cameras are biased so that zero light still has small number of counts), background room light, background scattered light (either scattered secondarily off of condensed moisture in the flow or outside the wavelength of interest), and the desired signal (directly scattered Raman light). A set of background images were taken for all data sets (without significant difference between an image set taken with a lens cap on or without the laser on, i.e. the background room light was negligible) that was used to normalize for the electronic background and background room light. In image regions just above and below the laser sheet, the background scattered light was averaged in the vertical direction, and subtracted to correct for the background scattered light. Images were then corrected for the flat-field intensity. Images from the intensified camera (N_2) were then aligned and scaled to the unintensified camera pixel dimensions. The laser sheets are neither completely uniform in the vertical direction nor of the same intensity from shot-to-shot, so in an air region (44 mm wide), the corrected, flat nitrogen images were averaged in the horizontal direction, and both the air and hydrogen (background corrected) images were divided by the vertical array to normalize for the individual shot laser intensity and non-uniformity in the y-direction. These corrected images images are the signal I/I_0 in eqs. 1 and 2. Corrected signals could then be converted to mole fractions and temperatures at each pixel.

3.0 RESULTS AND DISCUSSION

Image sets were taken at 2-6 heights from the nozzle, for hydrogen between 48 and 63 K and 2-5 bar_{abs} just before the nozzle, as shown in Table 1. Some example image sets are shown in Fig. 2. The left and right frames of these image sets are the median profiles for 400 individual laser pulses at each of 5–6 heights from the nozzle. The nozzle was moved in 10 mm increments and the images at each height were stitched together to give the overall image. In the median images, this stitching is fairly smooth, being the least smooth towards the tops of the images. This is likely due to the fact that the air region for which the laser sheet intensity correction was calculated was presumed to be the far right 44 mm of the images, and there may have been some hydrogen in this region further from the nozzle. The amount of humid air entrained, and hence, background scattered light, is also higher further from the nozzle, causing more noise on these images. On average, both the three and 5 bar jets have warmed around 50 K and

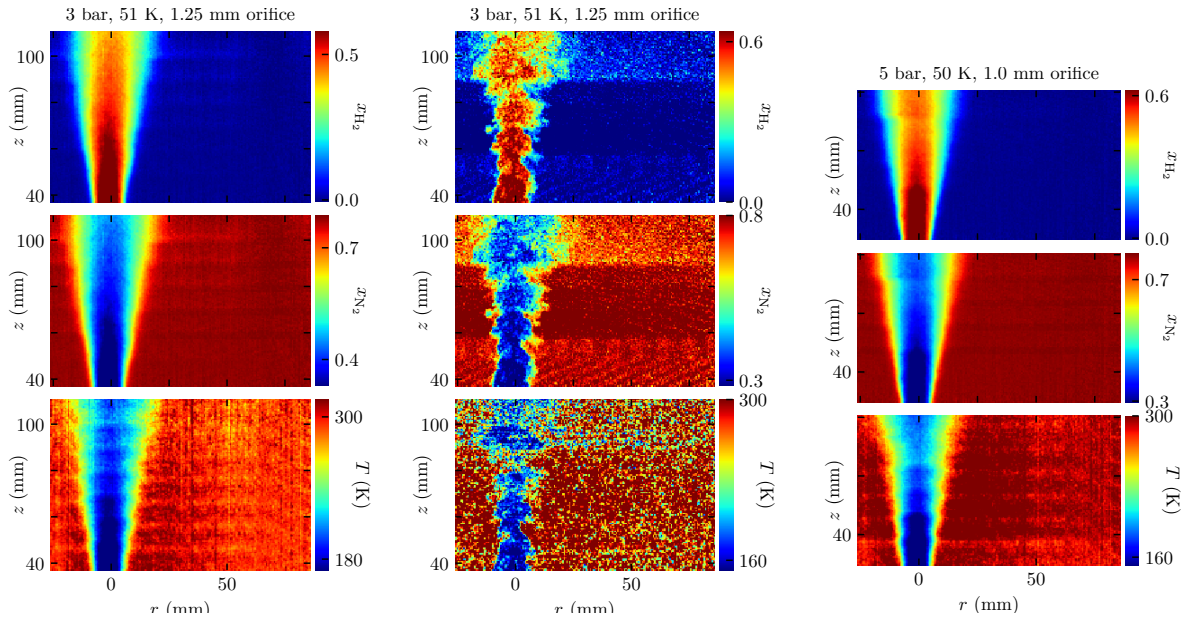

Figure 2. Profiles for mole fraction hydrogen (top frames), mole fraction nitrogen (middle frames), and temperature (bottom frames) for releases from a 1.25 mm orifice (left and center) and a 1mm orifice (right). Left and right image sets are median values from 400 images. Central is an analyzed image set for a single laser pulse at each imaging height.

the concentration of hydrogen has decayed by approximately 30% 40 mm downstream from the nozzle.

In the middle images of Fig. 2, one frame at each height is stitched together to form a complete image for mole fraction hydrogen, nitrogen, and temperature. In these images, there is significantly more noise than the median images on the left and right. However, these individual images show that these jets are in fact turbulent, with eddies of varying mole fraction and temperature. Comparing the individual mole fractions and temperatures in the middle images to the median mole fractions and temperatures on the left (for the same release conditions), we see that there are regions of the flow with mole fractions of hydrogen that are higher (and also lower) than the median mole fraction, and temperatures that are lower than the median temperature at a given location, due to the turbulence.

Figure 3 shows the variation in nozzle pressure and temperature (left frames) as the set of 400 images were being taken for each of 4–6 nozzle heights. The pressure, which was being controlled, shows very little variation and is steady at 2, 3, 4, and 5 bar_{abs}. These markers from pressure are similar to the markers for temperature, which are boxplots showing the 5^{th}, 25^{th}, 50^{th}, 75^{th} and 95^{th} percentage of the data. The temperature on the other hand, does have some variation, especially for the 5 bar_{abs} release. For the 5 bar_{abs} release, there is variation not only for each image set, but also at the different heights of the camera; the temperature varied by around 2 degrees when the camera was approximately 40 mm from the nozzle, and also on average by 4 degrees going from 40 mm to 80 mm. The density of 48 K hydrogen is nearly 10% higher than 52 K hydrogen, and the choked flow velocity is around 5% lower; errors which are slightly offsetting in terms of mass flow rate. This unsteadiness in the flows adds errors to the data, in addition to the errors associated with the noise on the cameras and the data processing techniques.

The right frames of Fig. 3 show the median centerline hydrogen mole fraction and temperature as a function of the distance from the 1 mm nozzle. The maximum hydrogen mole fraction and minimum temperature was observed to move laterally for some image sets, likely due to ice buildup near the nozzle. Rather than extracting the value of the mole fraction and temperature at the horizontal location 0 (see Fig. 2), the centerline temperature and hydrogen mole fraction in Fig. 3 are the maximum average mole fraction or minimum average temperature at each

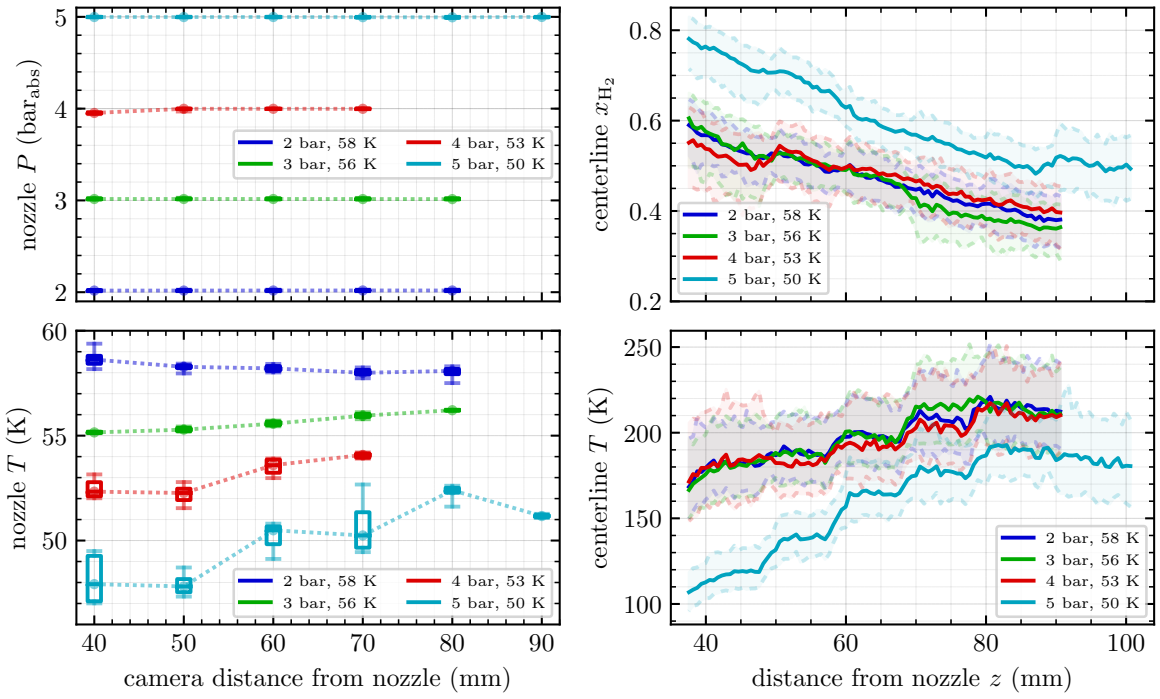

Figure 3. Nozzle pressure and temperature during data collection (left frames), and median centerline mole fraction and temperature (right frames) as a function of the distance from the nozzle, for the 1 mm orifice. In the left hand frames, the dashed line connects the median values while capturing images at each camera height, the boxes are the 25$^{\text{th}}$ and 75$^{\text{th}}$ quartiles, and the whiskers extend to the 5$^{\text{th}}$ and 95$^{\text{th}}$ percentage of the data. In the right-hand frames, the median centerline mole fraction or temperature are shown by the solid lines, while the shading proceeds out to dashed lines that capture the 25$^{\text{th}}$ and 75$^{\text{th}}$ quartiles of the data

height. This minimized the variation in the data where the different image sets were stitched together. Even with this definition of the centerline temperature or mole fraction, there are still some discontinuities observed in the data at some heights where the image sets are stitched together. The 4 bar release at approximately 50 mm from the nozzle, and 5 bar release around 85 mm from the nozzle are especially obvious for centerline mole fraction, and for nearly all of the stitched together imaging heights in terms of temperature. The trends in the centerline data are as expected, with decreasing mole fraction and increasing temperatures. The 2, 3, and 4 bar releases have very similar centerline mole fractions and temperatures, while the 5 bar release has the lowest temperature and highest centerline mole fraction. The shaded regions show the 25$^{\text{th}}$ and 75$^{\text{th}}$ quartiles of the mole fraction and temperature data. Some of these variations are due to noise on the data, but the majority of this spread is due to turbulent fluctuations in the flow (recall that the individual images look like the central images in Fig. 2).

The variation in nozzle pressure and temperature, and centerline mole fraction and temperature decay for the experiments with the 1.25 mm diameter nozzle are shown in Fig. 4. Similar to the data for the 1 mm orifice, the nozzle pressure during experiments was quite steady while there was up to 3 K variation in nozzle temperature. The mole fractions once again decay as the centerline temperature warms, moving away from the nozzle. There is a clearer trend of increasing centerline mole fraction and decreasing centerline temperature as the nozzle pressure (and hydrogen mass flow) increases for the 1.25 mm data than the 1 mm data. It is also easier to see in this case, that the variation in temperature and mole fraction (the width of the 25$^{\text{th}}$ and 75$^{\text{th}}$ quartiles) increases moving downstream in the flow.

Although there is some scatter in the data, the inverse average mass fraction at the release centerline decays linearly when the downstream distance is scaled appropriately, as shown in

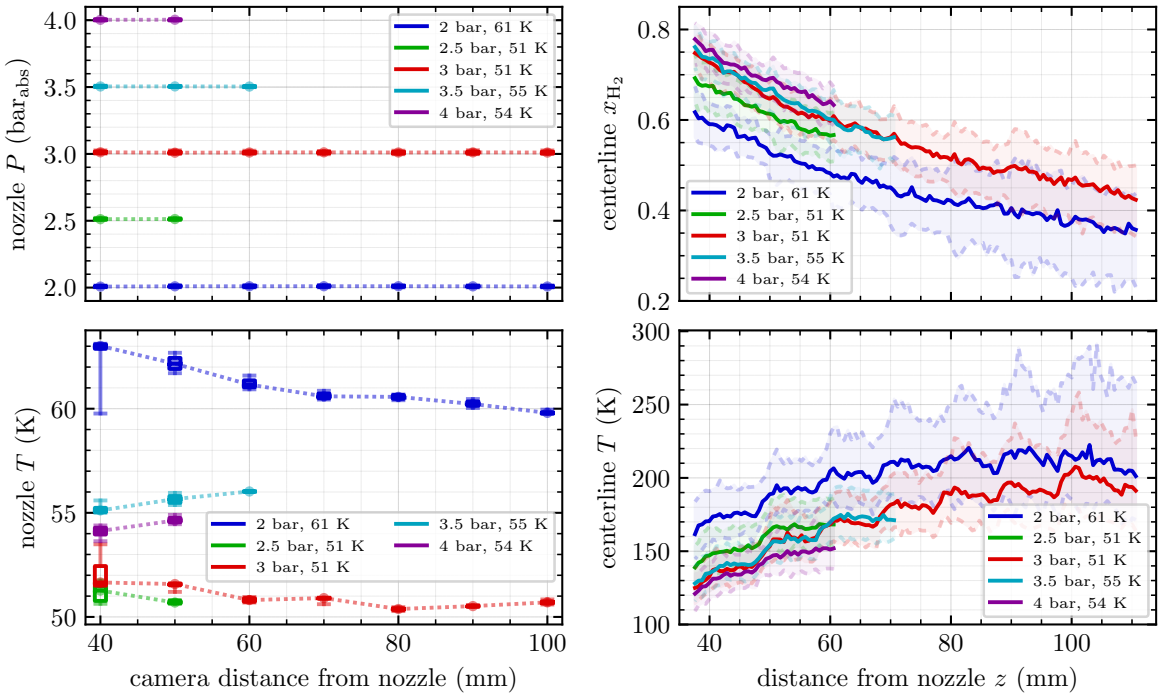

Figure 4. Nozzle pressure and temperature during data collection (left frames), and median centerline mole fraction and temperature (right frames) as a function of the distance from the nozzle, for the 1.25 mm orifice. In the left hand frames, the dashed line connects the median values while capturing images at each camera height, the boxes are the 25$^{\text{th}}$ and 75$^{\text{th}}$ quartiles, and the whiskers extend to the 5$^{\text{th}}$ and 95$^{\text{th}}$ percentage of the data. In the right-hand frames, the median centerline mole fraction or temperature are shown by the solid lines, while the shading proceeds out to dashed lines that capture the 25$^{\text{th}}$ and 75$^{\text{th}}$ quartiles of the data

the left frame of Fig. 5. The scaling factor is the effective diameter, $d\sqrt{\rho_0/\rho_a}$ where d is the nozzle diamter, ρ_0 is the nozzle stagnation density, and ρ_a is the room temperature and pressure air. This has been observed for a range of jet releases, as discussed by other researchers [11–13]. The decay rate has been measure to be as low as 0.21, or as high as 0.271. Our proportionality constant of 0.263 is within this range, implying that the centerline mass fraction is decaying at a similar rate to a room-temperature release. This is counter to an observation by Friedrich et al. [7], who found the inverse centerline mole-fraction decay rate to be slower than for room temperature releases, although there was significant scatter in their sparse concentration measurements.

In the right frame of Fig. 5, the jet half-width ($r_{1/2}$) is plotted as a function of the distance normalized by the nozzle radius. The half-width was found by fitting a Gaussian curve to each z pixel (each mm of height). The data collapses fairly well against this normalized downstream distance. As shown on the plot, the slope of the best-fit line for all of the data is 0.065 mm. For room temperature jets, this half-width decay rate has been found to be quite a bit faster–around 0.1 – 0.11 [11–13].

In order for the centerline mass fraction decay rate to be similar to, and the half-width decay rate to be less than their room temperature counterparts, and mass to be conserved in these flows, the velocity must also be different than for room temperature jets. These observations would suggest that the velocity decay along the centerline will be slower for cryogenic hydrogen than for warmer hydrogen. This will likely impact two empirical parameter in the model for these flows. First, the parameter that describes the ratio of the spreading of the velocity to the spreading of the concentration. The second is the empirically derived air entrainment rate–this may be a function of temperature, differentiating them from room temperature jets.

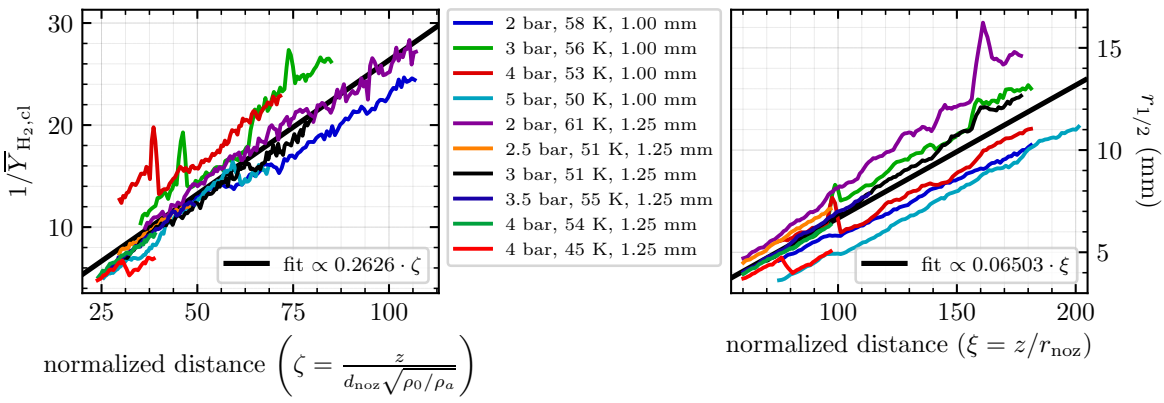

Figure 5. Centerline average inverse mass fraction decay (right) and mass fraction half-width (right) plotted as a function of the normalized downstream distance.

Figure 6 shows the data points at several downstream distances, along with three fits of a Gaussian curve for the normalized hydrogen mass fraction as a function of the normalized radius for all of the release conditions. The data collapses well using the normalization parameters of the average centerline hydrogen mass fraction, $\overline{Y}_{\mathrm{cl}}$ and the downstream distance, z. The red line in each plot is the Gaussian fit for the release conditions of each frame (at all heights, not just the selected heights in the legend). The 4 bar, 54 K, 1.25 mm diameter nozzle release is the most narrow, with a fit of $\overline{Y}/\overline{Y}_{\mathrm{cl}} = \exp(-64\eta^2)$, while the 3 bar, 56 K, 1 mm diameter nozzle release is the widest, with a fit of $\overline{Y}/\overline{Y}_{\mathrm{cl}} = \exp(-33\eta^2)$. The second Gaussian fit shown on the plot by the thick dashed black line is a fit to all of the different release conditions of this study. In some frames, this fit of $\overline{Y}/\overline{Y}_{\mathrm{cl}} = \exp(-49\eta^2)$ is slightly wider than the data, while in others,

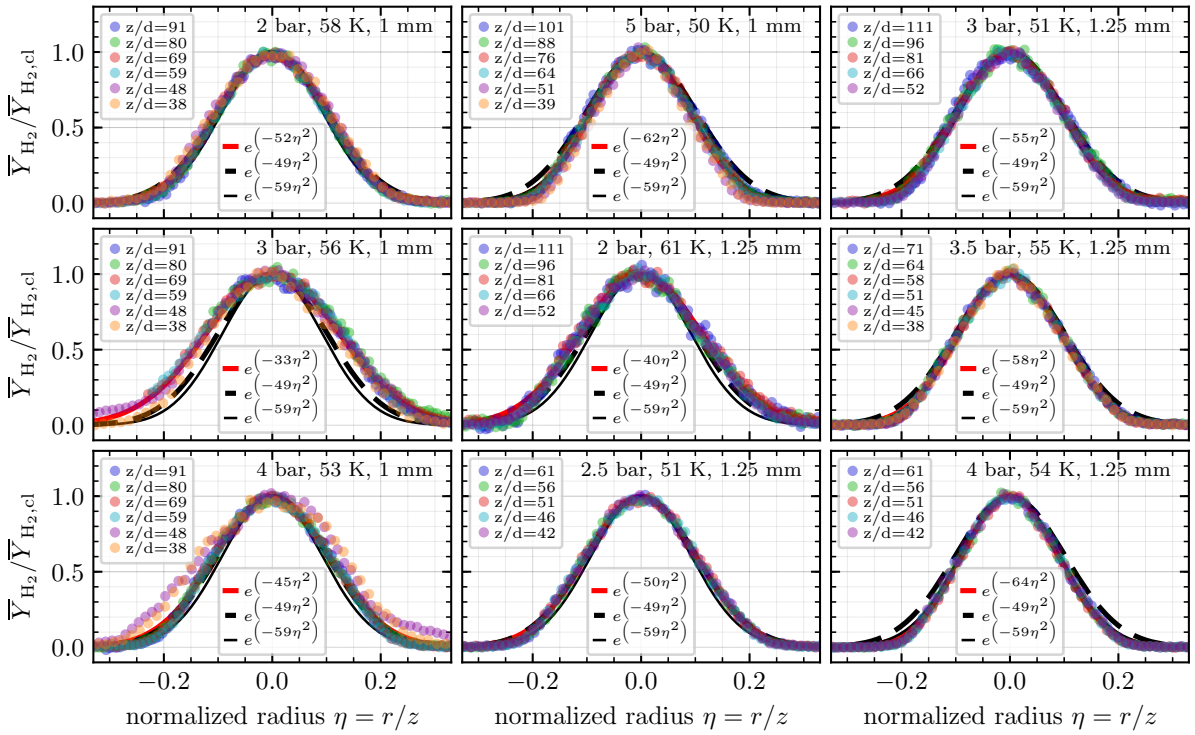

Figure 6. Radial mass fractions at selected distances, normalized by the centerline mass fraction. Three fits are shown on the graph. The red line is the fit for each condition (at all heights, not just the selected), the dashed thick black line is the fit for all 9 release conditions, and the thin black line is the literature fit [11, 14].

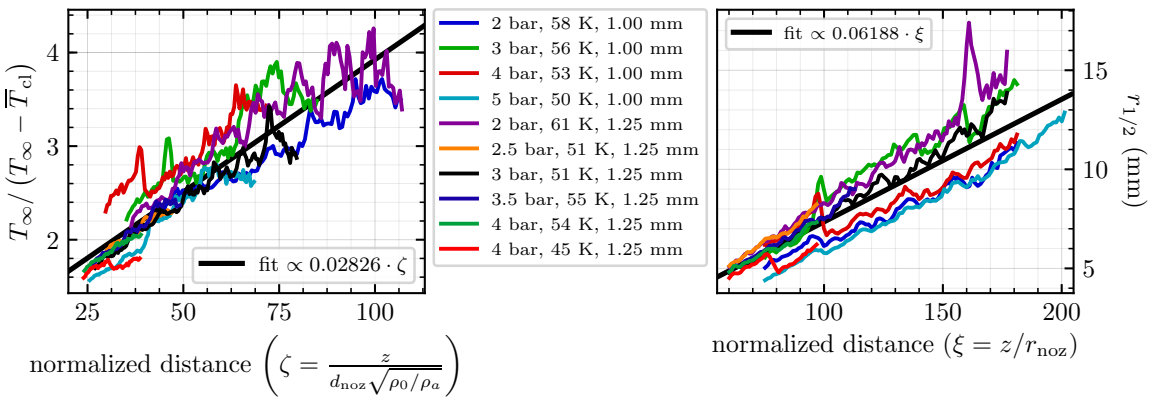

Figure 7. Normalized inverse centerline temperature decay (right) and temperature half-width (right) plotted as a function of the normalized downstream distance.

it is slightly narrower than the data, but overall does a fairly good job of predicting the radial mass fraction profile. The third line on the plot is the expected distribution from literature (for room temperature jets) of $\overline{Y}/\overline{Y}_{\mathrm{cl}} = \exp(-59\eta^2)$, shown by the thin black line [11, 14]. In most cases, this literature fit is narrower than the fit to the data of each frame.

The Raman scattering technique used in this study also allowed the measurement of temperature. Similar to Fig. 5, the normalized inverse average centerline temperature and half-width are plotted as a function of the normalized distance from the nozzle in Fig. 7. In this case, we are not aware of any literature data to which these decay rates can be compared. While comparing the inverse centerline average temperature decay rate to the inverse average mass fraction decay rate makes little sense because the normalization of the temperature is so much different from the inverse mass fraction, the half-width decay rates can be compared. In this case, the temperature half-width decays at a slightly lower rate of 0.062, than the mass fraction half-width decay rate of 0.065. One-dimensional modeling of jets (see e.g. [8, 9]) typically involves specifying the ratio of the half-width for different parameters (velocity, mole fraction, etc.) and this data will be used to better fit these models for cryogenic hydrogen jets.

Similar to the data of Fig. 6, the normalized mass fraction profiles are shown in Fig. 8. Three fits are also shown on these graphs. The red line is once again the Gaussian fit for the release conditions of each frame, and the thick dashed black line is the fit to the data for all 9 release conditions. The thin black line is once again the literature fit to the normalized mass fraction profile (since there was no equivalent literature data for temperature). The normalized temperature profiles are slightly wider than the mass fraction profiles. The coefficient in the Gaussian fits for normalized temperature range from 21–49, with a fit to all of the data of $\Theta = \exp(-42\eta^2)$. The atmospheric temperature, T_∞ was a parameter for the Gaussian fit, and the best-fit value ranges from 292-300 K. This is near the average lab temperature of 295 K, with the scatter due to challenges with data analysis and the amount of noise on the temperature profiles (see Fig. 2).

Finally, the data was compared to the ColdPlume model developed by Winters and Houf [8, 9] in Fig. 9. In some of these frames, the measured mole fraction and temperature fields at certain imaging heights were laterally offset significantly from the other imaging planes, likely due to ice at the nozzle. It should be noted that shifts out of the imaging plane are also likely in this setup, which will add error to the measurements. To correct for the lateral offset (no correction is possible for the out of plane offset), the maximum median mole fraction was determined, and the hydrogen, nitrogen, and temperature images were each shifted for each slice in the z-direction. Large shifts to the right of the images at some heights are especially evident for the 3 bar, 56 K, 1 mm release, where the experimental contours are jagged on the left hand side of the images. In most cases, the experimental contours for mole fraction are penetrating slightly further downstream than those predicted by the model. The widths of the mole fraction profiles are fairly well predicted by the model, and overall, the model is similar to the data.

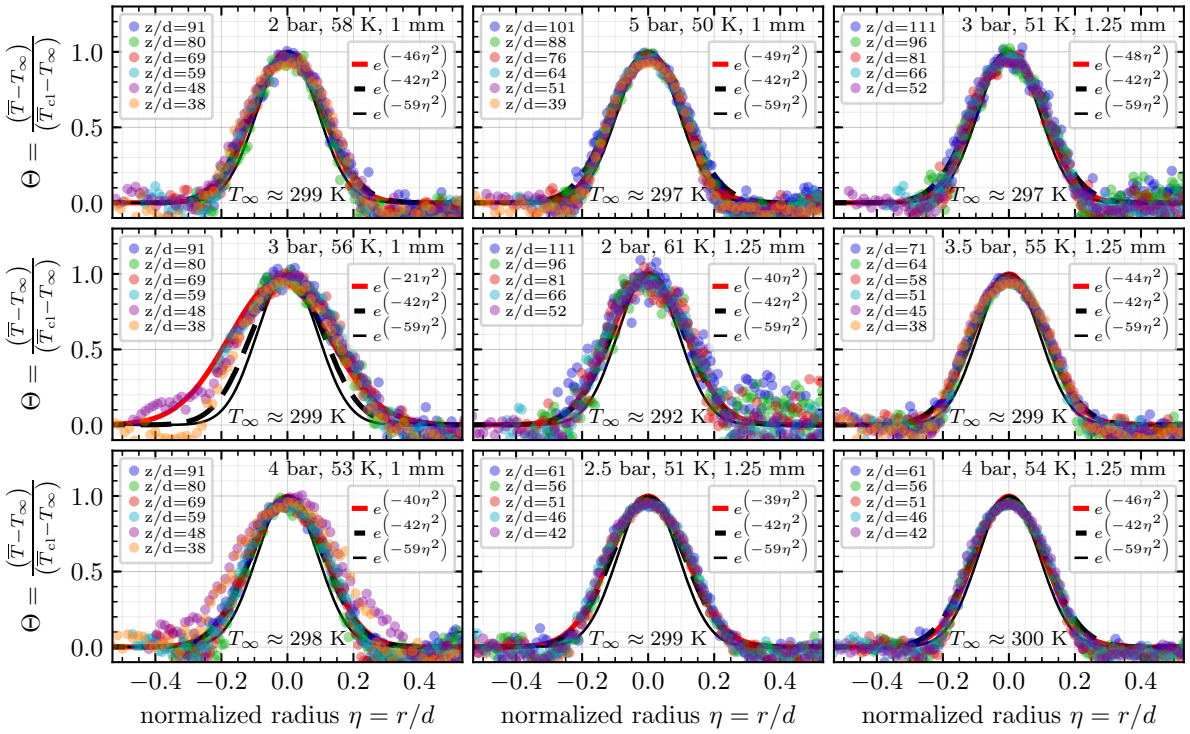

Figure 8. Radial temperatures at selected distances, normalized by the temperature excursion from the atmosphere. Three fits are shown on the graph. The red line is the fit for each condition (at all heights, not just the selected), the dashed thick black line is the fit for all 9 release conditions, and the thin black line is the literature fit for mass fraction [11, 14].

Cold temperatures, in Fig. 9b, do not seem to penetrate as far as predicted by the model, while the experimental temperature widths are similar to the model predictions. It is obvious in these contour plots that there is significant noise in the temperature data, and this additional noise should be taken into account during model validation.

4.0 CONCLUSIONS AND FUTURE WORK

Raman imaging was used to characterize unignited cryogenic hydrogen jets issuing through 1 and 1.25 mm diameter circular nozzles. Image sets were taken for nozzle pressures ranging from 2–5 bar_{abs} and nozzle temperatures ranging from 50–61 K. The concentration and temperature fields of these releases were measured, with individual images showing turbulent jets with eddies, and average profiles of 400 individual images. The average centerline mass fraction was observed to decay at a similar rate to room temperature releases of hydrogen, or other gases. The average half-width of the mass fraction jet, on the other hand, decayed more slowly than literature values of warmer jets. In order for mass to be conserved in models of these flows, empirical parameters such as the relative velocity and concentration profile spreading rates, and the entrainment rate will likely need to be modified from the values for warmer hydrogen. Radial profiles of the normalized hydrogen mass fraction and temperature show that these distributions are Gaussian and self-similar as a function of the radius normalized by the downstream distance. The normalized temperature is slightly wider than the normalized mass-fraction. Decay rates for the temperature magnitude and half-width were also measured in this work. Finally, the measured profiles were compared to a model. Both the measured temperature and mass fraction fields agreed with those predicted by the model, although improvements may be possible with empirical parameter adjustment.

We plan to use this data to modify the model and ensure accuracy for cryogenic hydrogen jets. We plan to evaluate the errors and error propagation in our data analysis before making

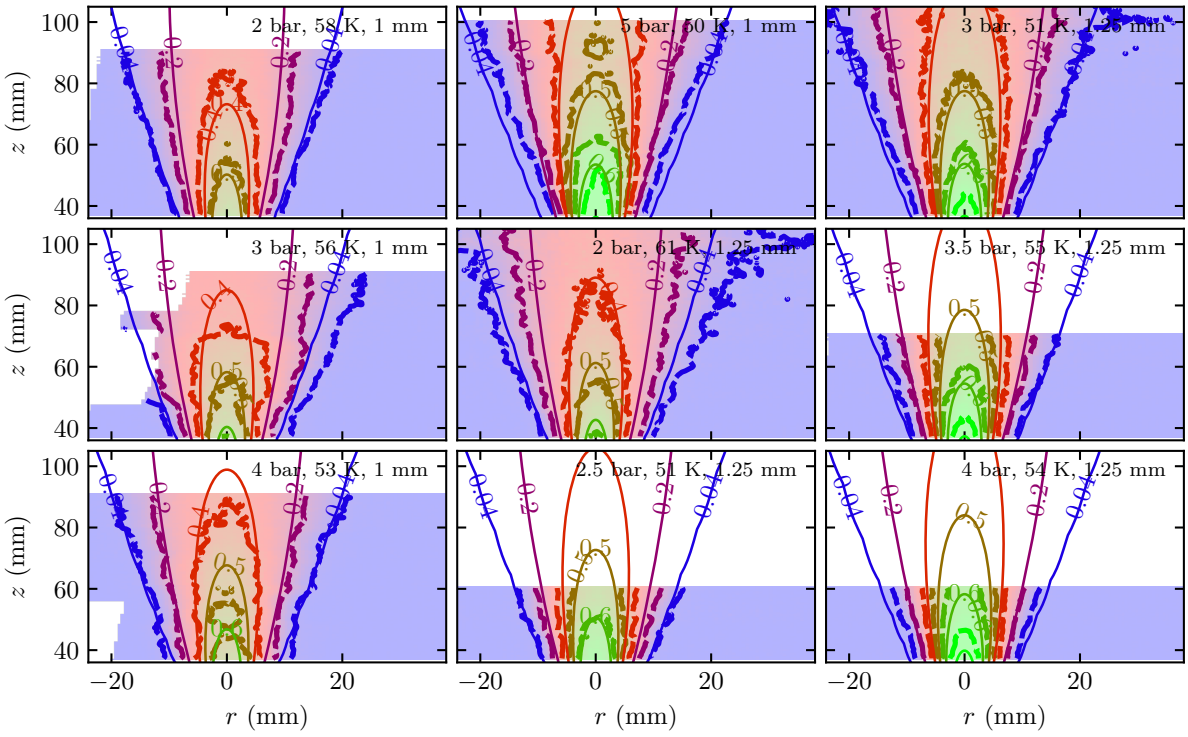

(a) Mole fraction fields. Contours are at mole fractions of 0.04 (the lean flammability limit for hydrogen), 0.2, 0.4, 0.5, and 0.6.

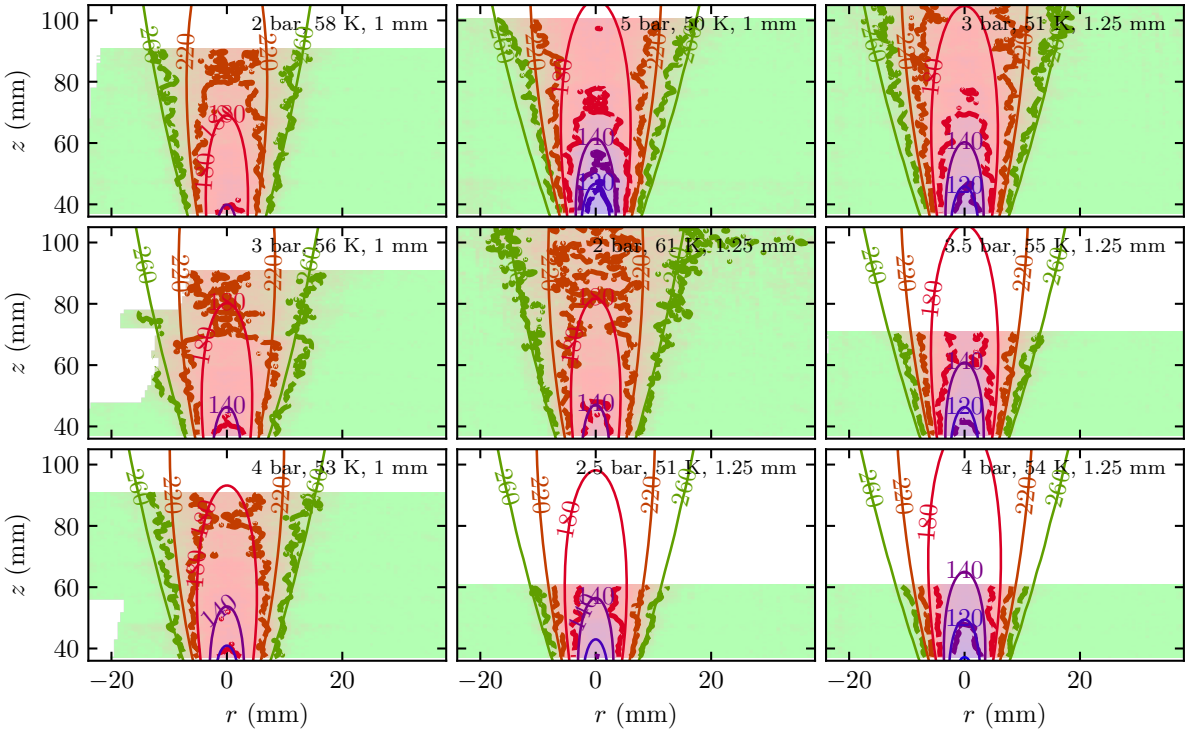

(b) Temperature fields. Contours are at 100, 120, 140, 180, 220, and 260 K.

Figure 9. Comparison of the model predictions shown by the solid, thin lines, to the experimental data, shown by the thick, dashed lines and shading for (a) mole fraction (top) and (b) temperature (bottom).

any modifications to the model. We also plan on taking data at lower temperatures, although air-icing around the nozzle does become troublesome, changing the trajectory of the release, at temperatures below 50 K. Icing at the nozzle can shift the release laterally, making stitching the images at different heights challenging and can shift the trajectory out of plane, such that we may not be measuring the jet across the centerline, causing challenges in data interpretation. Finally, we plan on attempting to measure velocity fields of these cryogenic jets using particle imaging velocimetry, potentially using the entrained moisture as the particle imaging medium.

ACKNOWLEDGEMENTS

The authors wish to than Radoslav Bozinoski for updating ColdPlume to a Python version. The U.S. Department of Energy's (DOE) office of Energy Efficiency and Renewable Energy's (EERE) Fuel Cell Technologies Office (FCTO) supports the development of science-based codes and standards through the Safety, Codes and Standards program element. The authors gratefully acknowledge funding from FCTO to support the work described in this report. Sandia National Laboratories is a multimission laboratory managed and operated by National Technology and Engineering Solutions of Sandia LLC, a wholly owned subsidiary of Honeywell International Inc. for the U.S. Department of Energy's National Nuclear Security Administration under contract DE-NA0003525.

REFERENCES

[1] 2016 Annual Evaluation of Hydrogen Fuel Cell Electric Vehicle Deployment and Hydrogen Fuel Station Network Development, Tech. rep., California Environmental Protection Agency Air Resources Board, available at https://www.arb.ca.gov/msprog/zevprog/hydrogen/hydrogen.htm (July 2016).
[2] NFPA 2: Hydrogen Technologies Code, Tech. rep., National Fire Protection Association (2016).
[3] J. LaChance, Risk-informed separation distances for hydrogen refueling stations, Int. J. Hydrogen Energy 34 (14) (2009) 5838–5845.
[4] J. LaChance, W. Houf, B. Middleton, L. Fluer, Analyses to support development of risk-informed separation distances for hydrogen codes and standards, Tech. Rep. SAND2009-0874, Sandia National Laboratories (2009).
[5] P. P. Panda, E. S. Hecht, Ignition and flame characteristics of cryogenic hydrogen releases, Int. J. Hydrogen Energy 42 (2017) 775–785.
[6] J. Xiao, J. Travis, W. Breitung, Hydrogen release from a high pressure gaseous hydrogen reservoir in case of a small leak, Int. J. Hydrogen Energy 36 (3) (2011) 2545–2554.
[7] A. Friedrich, W. Breitung, G. Stern, A. Veser, M. Kuznetsov, G. Fast, B. Oechsler, N. Kotchourko, T. Jordan, J. Travis, J. Xiao, M. Schwall, M. Rottenecker, Ignition and heat radiation of cryogenic hydrogen jets, Int. J. Hydrogen Energy 37 (22) (2012) 17589–17598.
[8] W. S. Winters, W. G. Houf, Simulation of small-scale releases from liquid hydrogen storage systems, Int. J. Hydrogen Energy 36 (6) (2011) 3913–3921.
[9] W. Houf, W. Winters, Simulation of high-pressure liquid hydrogen releases, Int. J. Hydrogen Energy 38 (19) (2013) 8092–8099.
[10] T. C. Williams, C. R. Shaddix, Simultaneous correction of flat field and nonlinearity response of intensified charge-coupled devices, Rev. Sci. Instrum. 78 (12).
[11] C. D. Richards, W. M. Pitts, Global density effects on the self-preservation behaviour of turbulent free jets, J. Fluid Mech. 254 (1993) 417.
[12] R. Schefer, W. Houf, T. Williams, Investigation of small-scale unintended releases of hydrogen: momentum-dominated regime, Int. J. Hydrogen Energy 33 (21) (2008) 6373–6384.
[13] A. J. Ruggles, I. W. Ekoto, Ignitability and mixing of underexpanded hydrogen jets, Int. J. Hydrogen Energy 37 (22) (2012) 17549–17560.
[14] A. J. Ruggles, Statistically advanced, self-similar, radial probability density functions of atmospheric and under-expanded hydrogen jets, Exp. Fluids 56 (11) (2015) 202.